Density-functional study of S_2^- defects in alkali halides

F. Stevens,[1] H. Vrielinck,[1] F. Callens,[1,*] E. Pauwels,[2] and M. Waroquier[2]
[1]*Ghent University, Department of Solid State Sciences, Krijgslaan 281 - S1, B-9000 Ghent, Belgium*
[2]*Ghent University, Laboratory of Theoretical Physics, Proeftuinstraat 86, B-9000 Ghent, Belgium*
(Received 23 April 2002; published 23 October 2002)

Density-functional methods, as implemented in the Amsterdam Density Functional program, are used to calculate the electron paramagnetic resonance (EPR) and electron nuclear double resonance (ENDOR) parameters of the S_2^- defect in a halide monovacancy in various alkali halides (MZ:M=Na, K, Rb and Z=Cl, Br, I) lattices. The calculations were performed on cluster in vacuo models for the defect and its lattice surroundings, involving up to 88 atoms in order to limit boundary effects. For all MZ lattices, the calculated g and ^{33}S hyperfine tensors of the S_2^- molecular ion are in very good agreement with the available EPR data, explicitly supporting the monovacancy model for the defect. In addition, computational results for the principal superhyperfine and quadrupole values and axes of the nearest shells of M^+ and Z^- ions are compared with experimental ENDOR data. The merits and shortcomings of the applied cluster in the vacuo method are critically evaluated.

DOI: 10.1103/PhysRevB.66.134103 PACS number(s): 76.30.Mi

I. INTRODUCTION

Since the late 1950s the superoxide molecular ion O_2^- has been the subject of numerous electron paramagnetic resonance (EPR) investigations in alkali halides (MZ:M=Na, K, Rb and Z=Cl, Br, I). Pioneering work has been done by authors of Refs. 1–3. This included both extensive experimental and theoretical work, in which formulas for g and hyperfine parameters were derived. The experimental data could be excellently described by this semiempirical method. Furthermore, the interactions with the six nearest cation neighbors (interactions 1 and 2, see below) were also discussed in a similar scheme.[2,3] In the mid sixties this EPR work was extended towards the S_2^-, Se_2^-, and SSe^- centers by the authors of Refs. 4–7. As will be explained below, the X_2^- (X=O,S,Se) centers have either a $^2B_{2g}$ or $^2B_{3g}$ ground state in the alkali halide lattice, apparently depending on the size of the chalcogen and the lattice ions. From Känzig and co-workers' theory this was reflected in differently oriented paramagnetic lobes of the unpaired electron. For both defect types a model in which X_2^- replaces a single Z^- ion was proposed (Fig. 1).

In the 1980s, however, by the use of new crystal growth methods, the centers mentioned above could be introduced in a growing number of alkali halide lattices.[8–17] The monovacancy model was questioned when in KCl a second S_2^- molecular ion was discovered, next to the one identified earlier in Refs. 5 and 8. The identification as S_2^- was in both cases carefully experimentally substantiated by, e.g., ^{33}S enrichment and testing to the theory of Känzig and co-workers. A divacancy model (S_2^- replacing two neighboring Cl^- ions along a $\langle 110 \rangle$ direction) was proposed (Fig. 2), also inspired by the larger number of anion vacancies introduced by the specific doping procedure.[8,9] From then onwards it was suspected that other X_2^- centers, especially the ''larger'' ones in ''smaller'' lattices, would also have to be (re)assigned to a divacancy site.

This ambiguity stimulated a lot of electron nuclear double resonance (ENDOR) work in the 1990s and finally in NaCl it could be unambiguously shown that S_2^-, Se_2^-, and SSe^- were present in a monovacancy site, suggesting that all molecular ions of this type could enter the alkali halides in a monovacancy configuration.[14–17] The KCl S_2^- case was left unsolved due to insufficient ENDOR data.

The occurrence of two different ground states and the call for an accurate model (monovacancy/divacancy) were the main objectives for the present density functional theory (DFT) study. The choice of the S_2^- ion (instead of O_2^-) to start such a study is due to two reasons.

(i) S_2^- in NaCl is the smallest defect for which the monovacancy model was proven experimentally.

(ii) Calculations on O_2^- have shown that the standard basis functions used in the Amsterdam density functional (ADF) program package are probably less accurate in describing the O_2^- molecular ion adequately.

The present *ab initio* DFT investigation of the S_2^- radical

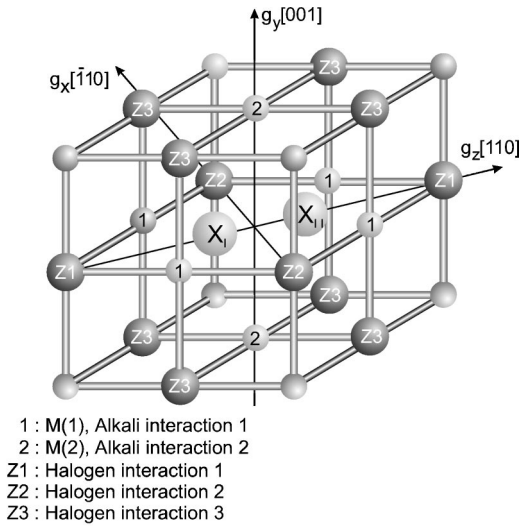

FIG. 1. Monovacancy model for the X_2^- molecular ion in alkali halides.

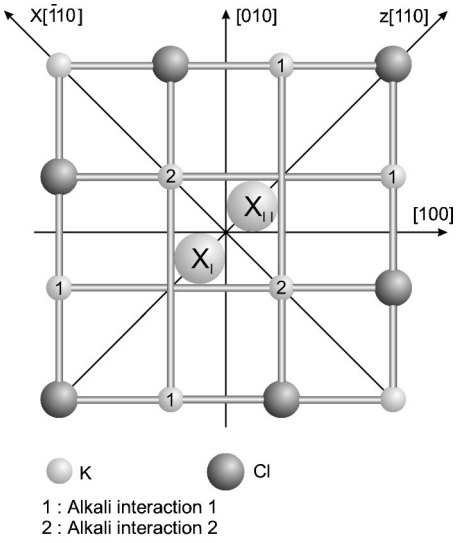

FIG. 2. Cross section of the divacancy model for the X_2^- molecular ion in alkali halides.

doped into different alkali halide lattices also intends to validate the DFT methods for the description of defects in ionic lattices. Using the monovacancy model, we shall try to reproduce the ground state of the S_2^- ion in the aforementioned nine lattices using the same modeling procedure. For this purpose, theoretical calculations have been carried out on clusters in vacuo, containing 88 atoms. Recent advances in computational chemistry have led to the development of new methods for the calculation of electronic g and hyperfine tensors. Most DFT-EPR studies focus on g and A tensor calculations for transition metal complexes,[18–26] defects in solids,[27–29] free radicals,[30–32] or organic molecules.[33–40] Although the merit of DFT methods in the calculation of hyperfine parameters of organic radicals is unquestionable, their adequacy to describe EPR parameters of more complex systems like transition metals or defects in solids is still almost unexplored.

The structure of the present paper is as follows. In Sec. II, the spin Hamiltonian parameters used in the analysis of the X_2^- defects in alkali halides are introduced and a short survey of the theory of Känzig and co-workers for these parameters is given. The computational details are summarized in Sec. III. Section IV is dedicated to the selection of the cluster. The quality of the spin Hamiltonian reproduction is tested on the S_2^- defect at a halide monovacancy in NaCl, for which the defect model was experimentally proven. In Sec. V, the DFT-EPR results for the nine MZ lattices are compared with experimental EPR and ENDOR results. The computational results are discussed in Sec. VI.

II. EPR PARAMETERS AND THE THEORY OF KANZIG FOR X_2^- LATTICE DEFECTS

In this section, we discuss briefly some general properties of EPR and ENDOR tensors. Also an introduction to the theory of X_2^- defects in NaCl-type lattices, as developed by in Refs. 1–3, is presented.

The theoretical principles of EPR and ENDOR are outlined in many textbooks,[41–44] and we only summarize the most relevant expressions. The spin Hamiltonian used for the interpretation of EPR and ENDOR spectra of systems with one unpaired electron (effective spin $S = \frac{1}{2}$) is given by

$$\hat{H}=\beta_e\hat{\vec{S}}\overline{g}\vec{B}-\sum_i \beta_N\hat{\vec{I}}_i\overline{g}_{N,i}\vec{B}+\sum_i \hat{\vec{S}}\overline{A}_i\hat{\vec{I}}_i+\sum_i \hat{\vec{I}}_i\overline{Q}_i\hat{\vec{I}}_i, \tag{1}$$

with $\beta_e=e\hbar/2m_e$ the Bohr magneton and $\beta_N=e\hbar/2m_p$ the nuclear magneton (m_e and m_p are the electron and proton mass, respectively).

The first term in this equation is the electronic Zeeman term, which describes the interaction between the electron spin $\vec{S}$ and the external magnetic field $\vec{B}$ and is parametrized by the g tensor. The second term is the nuclear Zeeman term, which describes the interaction between the applied magnetic field $\vec{B}$ and a nuclear spin $\vec{I}_i$. This interaction is parametrized by the nuclear g tensor $\overline{g}_{N,i}$, which in most cases reduces to a scalar $g_{N,i}$.

The third term describes the interaction between the electron spin $\vec{S}$ and a nuclear spin $\vec{I}_i$ and involves the (super)hyperfine tensor $\overline{A}_i$. We will further indicate the interaction with the nuclei of the X_2^- molecular ion, which makes out the core of the paramagnetic defect, as hyperfine interactions and use the expression superhyperfine interactions for interactions with neighboring nuclei. The (super)hyperfine coupling or A tensor is often decomposed into two terms: $\overline{A}=A_{iso}\overline{1}+\overline{A}_{dip}$. The isotropic or Fermi contact term A_{iso} is related to the probability $|\psi(0)|^2$ of finding the electron at the nucleus

$$A_{iso}=\frac{2}{3}\mu_0 g_e\beta_e g_N\beta_N|\psi(0)|^2 \tag{2}$$

where μ_0 is the magnetic permeability in a vacuum and $g_e=2.002319$ the free electron g value. The anisotropic part $\overline{A}_{dip}$ of the hyperfine tensor is due to the interaction between magnetic dipoles and yields additional information about the wave function and local environment of the unpaired electron. From classical expressions of interacting dipoles at a distance r, the anisotropic components are derived as[41]

$$A_{\alpha,\alpha}=\frac{\mu_0}{4\pi}g_e\beta_e g_N\beta_N\left\langle\frac{3\alpha^2-r^2}{r^5}\right\rangle, \tag{3}$$

$$A_{\alpha,\beta}=\frac{\mu_0}{4\pi}g_e\beta_e g_N\beta_N\left\langle\frac{3\alpha\beta}{r^5}\right\rangle, \tag{4}$$

with $\alpha,\beta=x,y,z$.

The last term in the spin Hamiltonian is the nuclear quadrupole interaction parametrized by the quadrupole tensor Q_i ($I > \frac{1}{2}$). To first order, the EPR spectrum gives no information about this interaction. The quadrupole tensor describes the interaction between the electric quadrupole moment of the nucleus and electric field gradients, which are present.

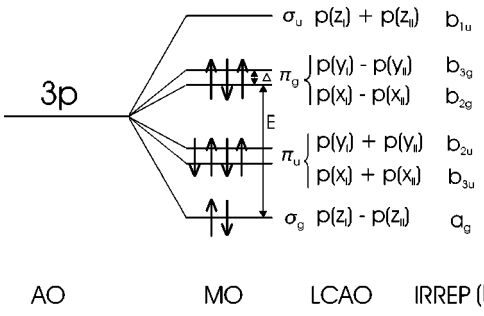

FIG. 3. Linear combination of atomic orbital (LCAO) energy levels scheme for the free S_2^- molecular ion and symmetry orbitals in a lattice field with D_{2h} symmetry. Also the irreducible representations (IRREP) for the considered symmetry group, atomic orbitals (AO) and molecular orbitals (MO) are shown.

The relation between the quadrupole tensor and the electrostatic potential V_i at the nucleus (i) is given by

$$Q_{(i),\alpha,\beta}=\frac{e\tilde{Q}}{2I(2I-1)}\frac{\delta^2 V_{(i)}}{\delta\alpha\delta\beta} \tag{5}$$

with $Q_{(i),\alpha,\beta}$ the representation of the nine elements of the Q tensor. $\tilde{Q}$ is the electric quadrupole moment of the involved nucleus. From this expression, it follows that the quadrupole coupling tensor is symmetric and has a zero trace.

The mentioned g, A (^{33}S hyperfine and superhyperfine) and Q tensors are characterized by three principal values and three principal axes. Especially in the case of superhyperfine and quadrupole tensors, the orientation of the principal axes can contain important information with respect to, e.g., the direction and distance of the interacting nucleus to the molecular defect center. Therefore, this orientational information will also be used in the discussion, which is certainly a great challenge for DFT calculations.

The free S_2^- molecular ion with $D_{\infty h}$ symmetry has a $(1\sigma_g)^2(1\sigma_u)^2(2\sigma_g)^2(2\sigma_u)^2$ $(3\sigma_g)^2(1\pi_u)^4(1\pi_g)^4(3\sigma_u)^2$ $(4\sigma_g)^2(4\sigma_u)^2(5\sigma_g)^2(2\pi_u)^4(2\pi_g)^3$ electron configuration, leading to a $^2\Pi_g$ ground state. In a NaCl-type lattice, the symmetry is lowered to D_{2h} and the orbital degeneracy of the π_g orbitals containing the unpaired electron is lifted: the $D_{\infty h}$ π_g level splits into a b_{2g} and b_{3g} level (Fig. 3). Depending on whether the unpaired electron resides in a b_{2g} or b_{3g} orbital, a $^2B_{2g}$ or $^2B_{3g}$ ground state arises. The two states are separated by an energy Δ. As shown by Zeller and Känzig,[2] the calculation of the principal g values involves also a third energy level with A_g symmetry and separated from the ground state by an amount of E. Also introducing an effective spin-orbit coupling constant λ, the principal g values were calculated to be

$$g_x=g_e\cos 2\varphi+(\cos 2\varphi-1+\sin 2\varphi)\frac{\lambda}{E},$$

$$g_y=g_e\cos 2\varphi+(\cos 2\varphi+1-\sin 2\varphi)\frac{\lambda}{E},$$

$$g_z=g_e\cos 2\varphi+2l\sin 2\varphi, \tag{6}$$

where z corresponds to the direction of the molecular axis which is along a $\langle 110\rangle$ crystallographic orientation in the considered alkali halides. The x direction is defined perpendicular to the axis ($\langle\bar{1}10\rangle$ direction) while the y axis is defined along the $\langle 001\rangle$ direction. The formulas (with $\tan 2\varphi=\lambda/\Delta$ and $l\approx 1$ a parameter to include covalency effects) as presented above show that $g_x<g_y$ and correspond to a $^2B_{2g}$ ground state, with the paramagnetic lobes [described in a lowest combination of atomic orbitals approximation by $p(x_I)$-$p(x_{II})$, $p(x_I)$ and $p(x_{II})$ denoting atomic p-orbitals on chalcogen nuclei X_I and X_{II} respectively] along $\langle\bar{1}10\rangle$. For the other ground state $g_y < g_x$ and the expressions for g_x and g_y have to be interchanged.

The formulas show that the free molecular ion has $g_x=g_y=g_\perp=0$ and $g_z=g_{//}=4$. For the formulas derived for the (super)hyperfine parameters we refer to Refs. 2 and 3.

III. COMPUTATIONAL DETAILS

All geometry optimizations and EPR calculations are based on DFT (Refs. 45–47) principles and were performed with the ADF program package,[48–50] version 1999. This program comprises a set of routines to evaluate g, A, and Q tensors as developed and implemented by van Lenthe.[51–53] The standard basis set IV was used in ADF,[54] employing Slater-type orbitals as basis functions. This corresponds roughly to a triple-ζ basis set extended with polarization functions for main group elements. Calculations were performed adopting the local density Approximation according to Vosko, Wilk, and Nusair's[55] parametrization of electron-gas data. Calculations with gradient-corrected functionals [Lb94,[56] PW91,[57] and Blyp (Refs. 58 and 59)] were performed but proved in bad agreement with experimental data.

All calculations were performed within the frozen core approximation.[49] For S, Cl, and Na, electrons up to the 2p shell were kept frozen while for Br, I, K and Rb, electrons up to the $3d$, $4d$, $3p$, and $4p$ shells respectively, were included in the core. With the zero-order regular approximation (ZORA) (Refs. 60–66) for relativistic effects one has a fast and powerful tool at hand to calculate the g, (super)hyperfine and the quadrupole tensor of systems containing heavy elements.

In the literature, there is no straightforward approach in calculating EPR tensors. EPR-DFT calculations on transition metal complexes are usually based on different methods for g and A tensor calculations:[22,25,26] g tensors are calculated using the spin orbit coupled spin-restricted ZORA Hamiltonian,[51] and hyperfine coupling parameters are obtained with the Scalar relativistic spin-polarized ZORA Hamiltonian.[67] As a test for the system under study, we performed g and A tensor calculations with the aforementioned and with the spin orbit coupled spin-unrestricted level of theory. Because the latter performed superior in all EPR calculations all results reported are based on this level of theory. The relativistic atomic potentials were calculated using the auxiliary program DIRAC,[68] which is supplied with the ADF program package.

TABLE I. Composition and definition of the cluster shells.

Shell	Member	Sublattic	No. of sites
1	100	M^+	6
2	110	Z^-	12
3	111	M^+	8
4	200	Z^-	6
5	210	M^+	24
6	211	Z^-	24
7	220	Z^-	12
8	221	M^+	24
9	300	M^+	6
10	222	Z^-	8

IV. SELECTION OF THE CLUSTER: COMPUTATIONAL STUDY OF S_2^- IN NACL

A. General considerations

In order to find the optimum cluster in vacuo model for the S_2^- defect in alkali halide lattices, structure optimizations were performed and spin Hamiltonian parameters were calculated for the defect in NaCl for several cluster sizes. As the spin Hamiltonian parameters strongly depend on relaxations of the surrounding lattice ions (this will be substantiated below), the cluster should be chosen sufficiently large, so that the displacements of the nearest alkali and halide shells have converged. Because the monovacancy model has been experimentally proven for S_2^- in NaCl, numerical agreement between calculated and experimental spin Hamiltonian parameters can be used as a second criterion in the selection of the cluster.

In Table I, the first few shells of cation (M^+) and anion (Z^-) neighbors around a single halide vacancy are defined. The clusters that we considered always consist of complete shells. As the influence of the rest of the lattice is totally neglected, it is to be expected that the best results will be obtained using clusters for which the total charge is minimal (i.e., ± 1, including the central S_2^- ion) and for which the electrostatic lattice potential at the halide vacancy (Madelung constant: 1.74758 for the infinite NaCl-type lattices[69]) is well reproduced. Clusters which meet these requirements and remain computationally tractable, consist of 26, 86, and 124 neighbor atoms of the S_2^- molecular ion. Their shell composition (SC), total charge (Q) and Madelung constant (MC) are given in Table II. In the following, the lattice relaxations and spin Hamiltonian parameters calculated for these clusters will be compared. In order to test whether the total charge and Madelung constant of the cluster are really important, calculations have also been performed on a 58-atom cluster, which does not meet the aforementioned requirements at all.

TABLE II. Shell composition (SC), total charge (Q) and Madelung constant (MC) for different cluster sizes, with NON the number of neighboring ions $+2$.

SC	NON	Q	MC
1–3	28	1	2.133
1–5	58	19	9.866
1–6,9	88	1	2.068
1–8,10	126	-1	1.516

B. Lattice relaxations

Structure optimizations were performed varying the S-S distance of the S_2^- ion and the positions of all Na^+ ions in shell 1 and all Cl^- ions in shell 2, while all other ions were kept at their undisturbed lattice position. We will justify our choice of the number of relaxed atoms below. Optimization of the defect-free lattice (Cl^- at the central halide vacancy) yielded no significant difference from the equilibrium Na - Cl distance (2.82 Å). Figure 4 presents the calculated S-S distance and the displacements of the nearest Na^+ and Cl^- ions as a function of the cluster size.

The S-S distance [Fig. 4(a)] appears to exhibit a complex dependence on the cluster size: it does not converge in a monotonic way. It should however be noted that the maximum variation found in this parameter barely exceeds 0.03 Å and that for the largest two clusters the difference is smaller than 0.007 Å. It is thus reasonable to assume that for the latter two clusters, the calculated S-S distance approximates the value for the infinite lattice very well. Because the S_2^- molecular ion is considerably larger than the Cl^- ion it replaces, the neighbor atoms which are allowed to relax (shell 1-2), mainly undergo an outward relaxation, i.e. a displacement along the axis interconnecting the center of the S_2^- and the neighbor ion, away from the center of the defect. These displacements are indicated with full dots in Figs. 4(b)–4(f). In general, it tends to decrease as the cluster size increases, indicating that an increasing number of fixed lattice points tends to prevent relaxing ions from being displaced. Symmetry allows that the first shell Na^+ ions in the equatorial g_z-g_x plane (indicated by 1 in Fig. 1) and the second shell Cl^- ions, not located in the equatorial plane (indicated with Z3 in Fig. 1) undergo additional displacements. These are indicated with open symbols in Fig. 4(b) and 4(f), and are in general much smaller than the outward relaxation. For the Na(1) [Fig. 4(b)], Na(2) [Fig. 4(c)], and Cl(1) [Fig. 4(d)] ions, the outward relaxation has clearly converged with cluster size. The deviant Na(2) displacement for the 58-atom cluster [Fig. 4(c)] is probably related with the deviant charge and Madelung potential of the cluster. For the other displacements, convergence is not yet reached at the largest cluster size. As the calculated spin Hamiltonian parameters are believed to be strongly dependent on the exact position of the neighboring atoms, these results suggest that improvement of the DFT-EPR results may still be expected by increasing the cluster size, even over 126 atoms. It may further be noted that the Na(1) ions [Fig. 4(b)] undergo the largest relaxation. The displacements for the second shell Cl^- ions [Figs. 4(d)–4(f)] are, however, of the same order of magnitude. This already indicates that the relaxations of the second shell ions should not be neglected. The outward relaxations of the $Z(1)$ ions [Fig. 4(d)] appear to be induced by the S_2^- molecular ion. A comparison of Figs. 4(b) and 4(e) suggests that the outward relaxation of the halides $Z2$ are

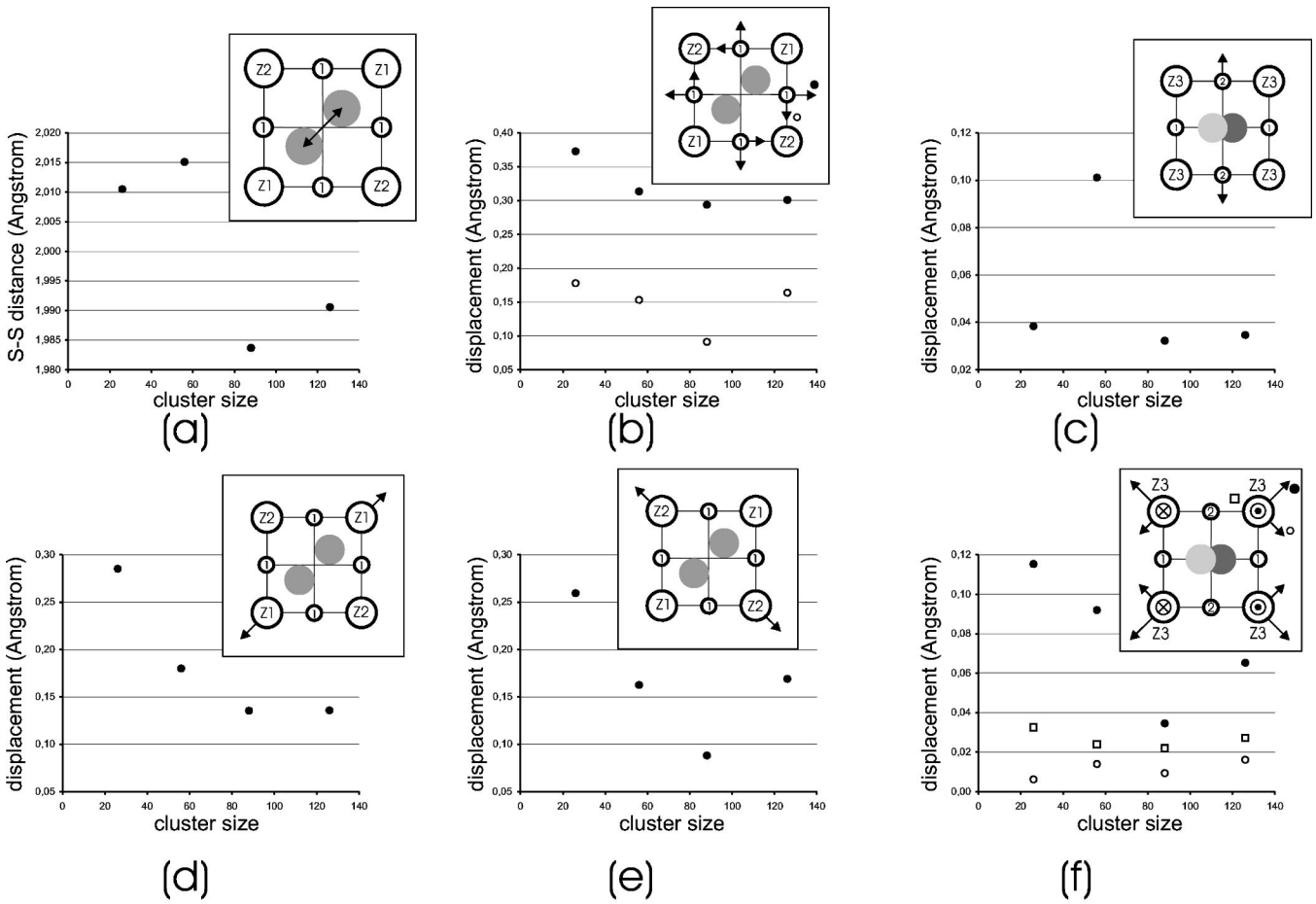

FIG. 4. Relaxations of the first two lattice shells as a function of the cluster size. The outward displacement of the S_2^- molecular ion is shown in (a). The directions and the magnitude of the relaxations for the first lattice shell ions (ions 1 and 2) are shown in (b) and (c) respectively. The relaxations of the ions of the second lattice shell: $Z1$, $Z2$, and $Z3$ are shown in (d), (e), and (f) respectively.

mainly due to the displacements of the Na(1) ions perpendicular to their outward relaxation.

C. Spin Hamiltonian parameters

For all optimized clusters, spin Hamiltonian parameters were calculated using the ADF program. Unfortunately, these calculations were computational not possible for the 126-atom cluster, which is hence no longer included in the comparison. The results for the other clusters are summarized in Figs. 5(a), 5(b), and 6 and Tables III and IV. For the neighbor interactions, data are only presented for the first shell Na^+ interactions Na(1) and Na(2), because only for these the comparison with experimental ENDOR data can be made. The experimental values are indicated in the figures as full lines.

Considering the g tensor [Figs. 5(a) and 5(b)], it is striking that for all luster sizes the correct ground state $({}^2B_{3g}, g_y < g_x < g_z)$ is obtained. If we compare the g values for the different cluster sizes with the experimental values, it is clear that the 58-atom cluster performs the poorest. This emphasizes the importance of the total charge and the electrostatic potential at the S_2^- site. Disregarding the values for the latter cluster, the calculated g values appear to converge towards the experimental data when the cluster size is increased. In fact, the agreement with experiment is already very satisfactory for the 88-atom cluster. Figure 7 shows the influence of the number of lattice shells that are allowed to relax on the calculated g values, using the 88-atom cluster. In order to obtain good numerical agreement, displacements of both the first shell Na^+ and the second shell Cl^- ions need to be considered. It should be noted that the correct ground state is predicted for the S_2^- ion, even if no neighbor relaxations are taken into account.

For all cluster sizes, the calculated ^{33}S hyperfine tensor is qualitatively in agreement with experiment (Fig. 6): the largest principal A value is found along the g_y direction and the other principal values are much smaller. Although the quantitative agreement improves when going from a 26- an 88-atom cluster (the 58-atom cluster again performs badly), even for the largest cluster the calculated value still largely deviates from the experimental A_y value. This discrepancy has also been noticed by Van de Walle and Blochl.[70] In this work, however, pseudopotentials have been implemented in the DFT concept, in order to handle defects which are unmanageable within all-electron calculations. For the S_2^- defects, there is no need for applying pseudopotentials, and we systematically perform full ab-initio calculations.

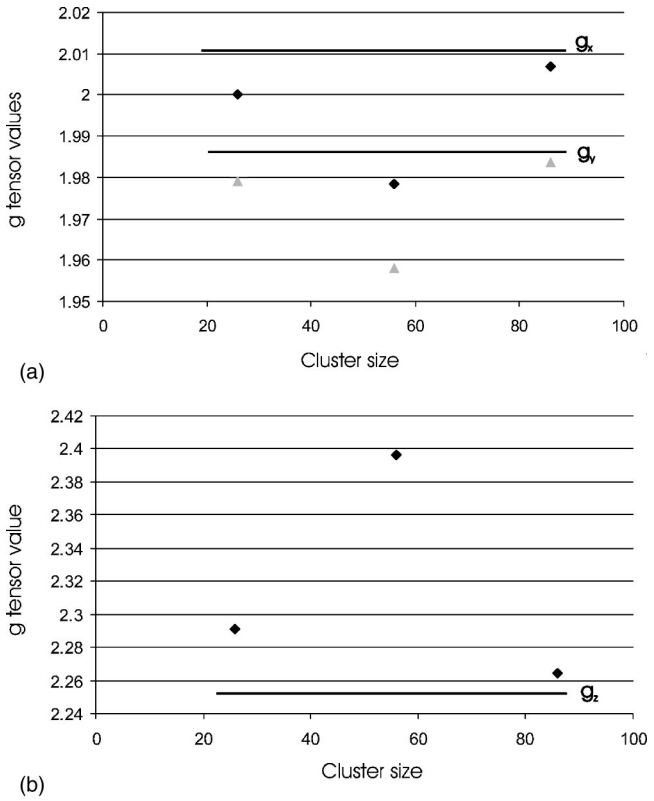

FIG. 5. Comparison of calculated and experimental g_x and g_y values (a) and g_z values (b) as a function of the cluster size. The experimental values are indicated as full lines in both figures.

In Table III, the calculated superhyperfine parameters for interaction Na(1) are presented. In order to eliminate problems in calculating the isotropic part of the interaction, the isotropic and anisotropic part of the tensors are compared with experiment separately. An additional parameter for this interaction is the tilting angle α in the g_z-g_x plane, between the A_z and g_z principal axes. In general, the agreement between calculated and experimental values is very poor. Independent of the cluster size, the calculated isotropic superhyperfine value is at least one order of magnitude too small. The anisotropic A values appear to improve when increasing the cluster size and reasonable agreement with experiment is obtained for the 88-atom cluster. The tilting angle, on the other hand, does not seem to improve in a monotonic way when the cluster size increases. It appears that none of the superhyperfine tensor characteristics of this interaction have converged yet and larger clusters (or other methods to incorporate the effect of the rest of the lattice) need to be considered in order to obtain even qualitative agreement with experiment. The results for the Na(1) Q tensor on the other hand, seems to improve clearly with increasing cluster size. For the 88-atom cluster, the tilting angle of this tensor practically equals the experimental value, while the principal values are slightly underestimated by a factor 2, but show good qualitative agreement with experiment. For interaction Na(2) (Table IV), the correspondence between experimental and calculated A parameters is again rather poor and does not seem to improve significantly by taking larger clusters. The results for the Na(2) Q tensor, on the other hand, seem to improve clearly with increasing cluster size.

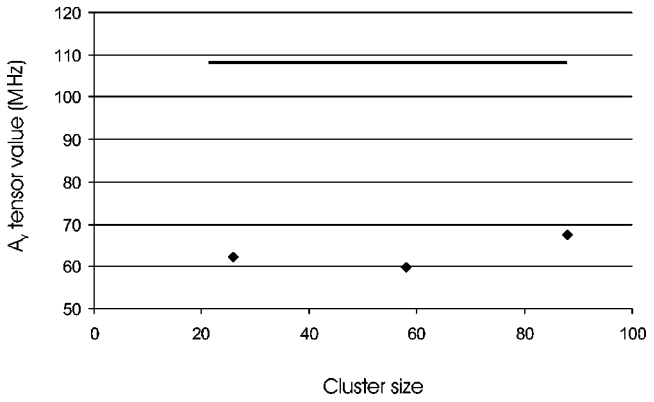

FIG. 6. Comparison of calculated and experimental (full line) A_y tensor value as a function of the cluster size. All values are in MHz.

TABLE III. Calculated superhyperfine and quadrupole parameters (MHz) for Na(1) as a function of cluster size. A_y and Q_y [001]. $\alpha_A(\alpha_Q)$, given in degrees, are the angles between the A_z (Q_z) and g_z principal directions A_{iso} stands for isotropic part, while $A_{i,\text{aniso}}$ $(i=x,y,z)$ stands for the anisotropic part of the A tensor.

	28	58	88	exp[a]
$A_{x,\text{aniso}}$	−0.43	−0.59	1.03	0.57
$A_{y,\text{aniso}}$	−0.51	−0.36	−0.56	0
$A_{z,\text{aniso}}$	0.94	0.95	−0.47	−0.57
A_{iso}	−0.11	−0.38	−0.09	3.91
α_A	76.3	0.1	9.8	54.8
Q_x	0.09	0.18	−0.22	−0.53
Q_y	−0.01	0.17	0.09	0.23
Q_z	−0.08	−0.35	0.13	0.3
α_Q	−87.5	−51.4	−32.1	−35.9

[a]Reference 9.

D. Choice of the cluster

The DFT-EPR results for S_2^- in NaCl indicate that, in order to obtain good quantitative agreement with experimental g values, relaxations of the first two neighboring shells

TABLE IV. Calculated A and Q tensor values (MHz) for Na(2) as a function of the cluster size. A_{iso} stands for the isotropic part, while $A_{i,\text{aniso}}$ $(i=x,y,z)$ stands for anisotropic part of A tensor.

	28	58	88	exp[a]
$A_{\text{x,aniso}}$	−0.91	0.87	−0.94	−0.94
$A_{\text{y,aniso}}$	0.99	0.99	1.04	0.36
$A_{\text{z,aniso}}$	−0.07	−0.11	−0.09	0.59
A_{iso}	−0.02	−0.03	−0.02	−4.41
Q_x	−0.053	0.041	−0.004	0.003
Q_y	0.121	0.052	0.023	−0.007
Q_z	−0.068	−0.093	−0.019	0.004

[a]Reference 9.

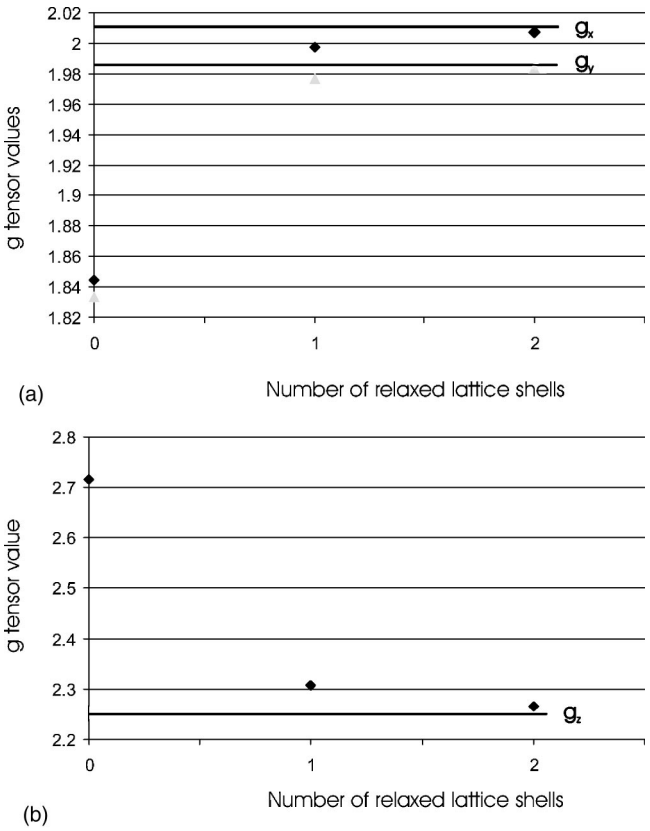

FIG. 7. Comparison of calculated and experimental g_x and g_y values (a) and g_z values (b) as a function of the number of neighbor shells that are allowed to relax. The experimental values are indicated as full lines in both figures.

should be considered. Furthermore, the selected cluster should have a low total charge and the Madelung potential at the central halide monovacancy should be well reproduced. Structural optimizations, on the other hand, demonstrate that even for the largest clusters we considered (up to 126 atoms) not all relaxations of the first two neighboring shells have converged yet. Therefore, increasing the cluster size is still expected to have an important positive influence on the quantitative agreement between experimental and calculated spin Hamiltonian parameters.

The largest cluster, meeting the aforementioned requirements of total charge, Madelung potential, and number of relaxed neighboring shells, for which the DFT-EPR calculations are computational achievable, is the 88-atom cluster. In Sec. V this type of cluster is used to calculated the spin Hamiltonian parameters of S_2^- in the other MZ lattices, in order to evaluate the monovacancy model for the defect. From the results for the NaCl lattice, we expect quantitatively good agreement with the experimental g values and qualitatively good agreement for the ^{33}S hyperfine tensor if the monovacancy model is correct. For neighbor interactions, only for the ligand quadrupole tensors good qualitative agreement with experiment may be expected.

V. MONOVACANCY MODEL FOR THE S_2^- DEFECT IN ALKALI HALIDES

A. EPR parameters

Following the procedures outlined in Sec. IV, geometry optimizations and calculations of spin Hamiltonian parameters were carried out for the other lattices. In Table V, the calculated and experimental g values for the nine lattices are compared. In all alkali halides where only one S_2^- defect was observed, calculations predict the correct ground state: in the sodium halides, KBr and KI, the S_2^- ion has the $^2B_{3g}$ ground state and in the rubidium halides, it has the $^2B_{2g}$ ground state. Calculated and experimental ^{33}S hyperfine values are listed in Table VI.

For the NaZ lattices, the agreement between calculated and experimental g tensors is nearly perfect. The observed trends in the principal g values with growing ionic radius of the halide ion (g_x and g_y increase, while g_z decreases) are

TABLE V. Comparison of the calculated principal g values with experimental values. For all lattices, the corresponding ground state (GS) is listed.

	Experimental			Theoretical			
lattice	g_x	g_y	g_z	g_x	g_y	g_z	GS
NaCl[a]	2.0107	1.986	2.2531	2.0069	1.9837	2.2643	$^2B_{3g}$
NaBr[b]	2.0114	1.9876	2.2379	2.0135	1.9955	2.2684	$^2B_{3g}$
NaI[c]	2.0178	1.9942	2.2303	2.0162	2.0005	2.2478	$^2B_{3g}$
KCl[c]	0.9484	0.95	3.4303	0.4641	0.4654	3.8206	$^2B_{2g}$
KCl[d]	1.9708	1.9491	2.4548				$^2B_{3g}$
KBr[c]	0.8434	0.8388	3.5037	0.8501	0.8481	3.6507	$^2B_{3g}$
KI[c]	1.6369	1.6254	3.0629	1.3125	1.3053	3.4036	$^2B_{3g}$
RbCl[e]	1.8728	1.8881	2.6515	1.1678	1.1751	3.5344	$^2B_{2g}$
RbBr[c,e]	1.7448	1.7571	2.8936	1.0574	1.0635	3.6464	$^2B_{2g}$
RbI[c]	1.2895	1.2968	3.3595	0.3925	0.3935	3.8635	$^2B_{2g}$

[a]Reference 9.
[b]Reference 12.
[c]Reference 6.
[d]Reference 8.
[e]Reference 13.

TABLE VI. Comparison of the calculated principal A values (MHz) with experimental values.

	Experimental			Theoretical		
lattice	A_x	A_y	A_z	A_x	A_y	A_z
NaCl[a]	$<A_z$	108.5	$<A_z$	−28.7	67.4	−10.3
NaBr	n.a.	n.a.	n.a.	−27.4	62.7	−10.7
NaI	n.a.	n.a.	n.a.	−28.8	63.9	−15.2
KCl[b]	$<A_z$	$<A_z$	137	5.6	2.9	152.4
KCl[c]	19.4	99.9	32.8			
KBr[b]	$<A_z$	$<A_z$	145	2.8	12.1	129.3
KI[b]	$<A_y$	64	93	−0.7	24.3	101.8
RbCl	n.a.	n.a.	n.a.	22.8	0.4	114.2
RbBr	n.a.	n.a.	n.a.	20.6	1.8	129.9
RbI[b]	$<A_z$	$<A_z$	105	4.3	2.4	144

[a]Reference 9.
[b]Reference 6.
[c]Reference 8.

TABLE VII. Experimental and theoretical isotropic A and Q tensor values (MHz) of the Na(1) interaction. A_{iso} stands for the isotropic part, while $A_{i,\text{aniso}}$ $(i=x,y,z)$ stands for the anisotropic part of the A tensor. The angles α_A and α_Q are in degrees.

	Experimental			Theoretical		
	NaCl[a]	NaBr[b]	NaI[b]	NaCl	NaBr	NaI
$A_{x,\text{aniso}}$	0.57	0.47	0.41	1.04	0.92	0.81
$A_{y,\text{aniso}}$	0	0.11	0.21	−0.56	−0.47	−0.44
$A_{z,\text{aniso}}$	−0.57	−0.58	−0.62	−0.48	−0.45	−0.37
A_{iso}	3.91	3.48	2.99	−0.09	−0.08	−0.07
α_A	54.8	55.5	54.3	9.8	19.9	25.3
Q_x	−0.53	−0.41	−0.28	−0.22	−0.16	−0.08
Q_y	0.23	0.17	0.12	0.09	0.07	0.03
Q_z	0.3	0.24	0.16	0.13	0.09	0.05
α_Q	−35.9	−36.3	−33.6	−32.1	−32.9	−26.8

[a]Reference 9.
[b]Reference 16.

very well reproduced by the calculations. Experimental hyperfine data are only available in the NaCl case. The agreement with the calculations has already been discussed in Sec. IV C. For the NaBr and NaI lattices, the DFT results predict the same qualitative result as for NaCl: $A_y \gg A_x$, A_z. From these computational results, little doubt is left that the monovacancy model is correct for all three lattices.

The experimental g values for S_2^- in KBr and KI exhibit a much larger deviation from g_e than those in the sodium halides. This is also nicely reproduced by the calculations. The agreement with experiment is not quite as good as for the NaZ lattices, but is still very satisfactory. The hyperfine values are again qualitatively in very good agreement with experiment and the quantitative agreement seems to be better than for the NaZ lattices. Calculations predict that $A_z > A_y > A_x$. Also for these two lattices, the computational results strongly support the monovacancy model.

For the RbZ lattices, the overall quantitative agreement between calculated and experimental EPR parameters is not so good. Experimental trends in the principal g components as a function of the halide ionic radius (a decrease of g_x and g_y, and an increase of g_z), are very well reproduced by the calculations on the other hand. It should be noted that we encountered computational difficulties for the RbI lattice. Therefore, we consider the results for this lattice to be less reliable. The calculations predict for all RbZ lattices that $A_z > A_x > A_y$, in contrast with the results for KBr and KI. The good qualitative agreement with experimental g and A data lead us to believe that also for these lattices the monovacancy model for the S_2^- defect is correct.

In KCl, finally, two S_2^- defects with different ground states have been experimentally encountered. Calculations predict the $^2B_{2g}$ ground state for S_2^- in a single halide vacancy. A comparison with the experimental EPR parameters of the S_2^- defect in the $^2B_{2g}$ ground state, reported by Vannotti and Morton[6] shows satisfactory agreement for the g values and even quantitatively good agreement for the hyperfine tensor. The monovacancy model thus appears very plausible for this defect. As for the RbZ lattices, in which S_2^- has the same ground state, according to the calculations $A_z > A_y > A_x$. The present results give no further information about the nature of the second S_2^- defect with the $^2B_{3g}$ ground state, reported by Callens *et al.*[8]

B. ENDOR parameters

1. Na-halide lattices

The principal values and tilting angles of the superhyperfine and quadrupole tensors of interaction Na(1) are given in Table VII. In general, the correspondence between experimental and calculated A tensors is bad, as was already discussed for the NaCl lattice. The isotropic superhyperfine values are much too small and have the wrong sign. At first glance, the anisotropic part of the A tensor appears to be better calculated. The poor agreement between experimental and calculated tilting angle indicates that also this part is not at all well reproduced. It was experimentally observed that the isotropic and all principal components of the anistropic superhyperfine tensor decrease when the halide ionic radius increases. This effect is well reproduced by the calculations. However, taking into account that all contributions to the superhyperfine tensor (Fermi contact interaction, point dipole interaction, covalency, and wave function overlap) decrease with increasing distance between the center of mass of the unpaired electron distribution and the interacting nucleus, this result is not at all surprising. The calculated quadrupole tensors are in much better agreement with experiment. If all calculated tensors were to be multiplied by a factor of 2–3, the agreement would even be excellent. The experimental trends observed when comparing the Q tensor characteristics of the three NaZ lattices are always reproduced, even for the tilting angle. For the interaction Na(2), the agreement between calculated and experimental superhyperfine values is again very poor (Table VIII). The calculated quadrupole values, on the other hand, would be in very good qualitative

TABLE VIII. Experimental and theoretical isotropic and anisotropic A and Q tensor values (MHz) of the Na(2) interaction. A_{iso} stands for the isotropic part, while $A_{i,aniso}$ $(i=x,y,z)$ stands for the anisotropic part of the A tensor.

	Experimental			Theoretical		
	NaCl[a]	NaBr[b]	NaI[b]	NaCl	NaBr	NaI
$A_{x,aniso}$	−0.94	−0.8	−0.63	−0.95	−0.71	−0.53
$A_{y,aniso}$	0.36	0.52	0.65	1.04	0.92	0.79
$A_{z,aniso}$	0.58	0.28	−0.02	−0.09	−0.21	−0.26
A_{iso}	−4.41	−3.55	−2.48	−0.02	−0.01	−0.02
Q_x	0.003	0.01	0.034	−0.004	−0.02	−0.028
Q_y	−0.007	−0.05	−0.086	0.023	0.05	0.067
Q_z	0.004	0.04	0.052	−0.019	−0.03	−0.039

[a]Reference 9.
[b]Reference 16.

agreement with experiment if the signs of the latter were to be reversed. The experimentally observed increase in the absolute value of the principal Q components with increasing halide ionic radius is very well reproduced by the calculations. This effect cannot be simply attributed to the increasing lattice parameter, as A and Q tensor components roughly exhibit the same dependence on the distance between the unpaired electron and the interacting nucleus. This leads us to believe that the calculations are, in spite of the lacking numerical agreement, very reliable and that the signs of the experimental principal components, which cannot be directly determined, should be changed.

For NaBr and NaI, the interaction with the eight equivalent second shell halide ions outside of the g_x-g_z plane has also been experimentally observed. These ions are indicated with $Z3$ in the model in Fig. 1. Symmetry imposes no restrictions on their principal A and Q orientations. Thus the superhyperfine tensor is determined by seven free parameters and the quadrupole tensor by six. In accordance with the literature, all three principal values and three direction cosines for each principal direction are given in Tables IX and X, wherein experimental and calculated A and Q tensor characteristics for the ^{79}Br and ^{127}I interactions are compared. Rather surprisingly, the agreement between experiment and calculations is very good. The isotropic superhyperfine values are very well reproduced. The anisotropic superhyperfine interaction of ^{79}Br is slightly overestimated, but the agreement between experimental and calculated principal directions is very satisfactory. For the ^{127}I interaction, the numerical agreement is nearly perfect. The principal quadrupole values for both ^{79}Br and ^{127}I are largely overestimated and the agreement between calculated and experimental axes is not quite as good as for the A tensors. Still the qualitative agreement with experiment may be called very satisfactory, especially if one considers that these ions are already very close to the edge of the cluster. Finally, it should be mentioned that the calculations predict that the superhyperfine interaction with the ^{79}Br and ^{127}I ions in positions $Z1$ and $Z2$ (see Fig. 1) is much smaller. This explains why these interactions were not identified in the ENDOR spectra.

2. RbCl

The ENDOR results for this lattice are discussed separately, because in this case the S_2^- ion has the $^2B_{2g}$ ground state. The experimental and calculated A and Q tensor values for the interactions Rb(1) and Rb(2) are listed in Tables XI and XII, respectively. One immediately observes a striking difference with the experimental and DFT results for S_2^- in the NaZ lattices, with the $^2B_{3g}$ ground state. For these lattices (or ground states), the absolute values of the principal superhyperfine components of interactions Na(1) and Na(2) have the same order of magnitude. Although the numerical agreement between experiment and calculations is rather poor, DFT-EPR reproduces this experimentally observed fact. For S_2^- in RbCl, both isotropic and anisotropic parts of the superhyperfine tensor of interaction Rb(1) are at least one order of magnitude larger than those of the Rb(2) interaction. The DFT calculations are in very good agreement with this experimental result, which is strongly related with the fact that the $^2B_{2g}$ unpaired electron orbital directly overlaps with the s and p orbitals of the alkali ligands in the g_z-g_x plane, whereas the Rb(2) ions are situated in a nodal plane of the $^2B_{2g}$ orbital. For the S_2^- in the $^2B_{3g}$ ground state, all first shell alkali ions are located in nodal planes of the unpaired electron orbital. The experimental and DFT results for the superhyperfine interactions are an additional indication in favor of the monovacancy model for S_2^- in RbCl, because, in a divacancy model, the overlap with the Rb(1) ions is not expected to be equally large.

The quantitative comparison between experimental and

TABLE IX. Experimental (Ref. 16) and theoretical halogen interaction (^{79}Br) of NaBr (MHz).

		Experimental angle between				Theoretical angle between		
		g_x	g_y	g_z		g_x	g_y	g_z
A_x	22.47	135	49	74.6	26.87	128.3	42.4	74.4
A_y	8.44	122.4	137.8	66	4.93	104.4	149.4	55.4
A_z	8.24	62.4	81.7	29	4.13	48.1	63.6	29.9
A_{iso}	13.05				11.98			
Q_x	−1.62	121.8	36.7	73.6	−4.82	135.2	0.4	45.2
Q_y	1.39	52.5	54	122.2	3.33	45.1	4.7	135.1
Q_z	0.23	126.4	96.2	142.9	1.49	93.1	94.8	176.3

TABLE X. Experimental (Ref. 16) and theoretical halogen interaction (^{127}I) for NaI (MHz).

		Experimental angle between				Theoretical angle between		
		g_x	g_y	g_z		g_x	g_y	g_z
A_x	22.04	133.1	48.6	71.9	19.25	138.6	48.6	70.6
A_y	8.53	91.9	117	27.1	6.96	91.9	115.1	25.2
A_z	7.68	43.2	53.3	70.6	4.26	34.9	59.5	74.4
A_{iso}	12.75				10.16			
Q_x	0.63	110.9	20.9	91.3	4.46	135.8	1.4	135.1
Q_y	−0.61	50.3	76.9	137.4	−2.99	41.8	71.6	137.5
Q_z	−0.02	133	106.1	132.6	−1.47	166.1	118.4	101.8

calculated spin Hamiltonian parameters for interaction Rb(1) shows very good agreement for the isotropic superhyperfine interaction and the tilting angles of both the *A* and *Q* tensors. The anisotropic *A* values appear to be underestimated by a factor of 2–3. The principal *Q* values show a good qualitative agreement. For interaction Rb(2), the calculations again underestimate the anisotropic superhyperfine values by approximately the same factor as for interaction Rb(1). The calculated isotropic *A* value and principal *Q* components are in poor agreement with experiment.

VI. DISCUSSION

The present study shows that DFT-EPR calculations of S_2^- defects in alkali halide lattices represent a successful tool in the reproduction of experimental EPR and ENDOR data. Nevertheless, we notice some discrepancies. We will focus on this aspect and report on some limitations of the present model and suggestions for substantive improvement. The size of the cluster turns out to be of great importance in the quantitative reproduction of a lot of EPR quantities.

Increasing the cluster size and the number of relaxing shells has shown to significantly improve the *ab initio* reproductions of the *g* and ^{33}S hyperfine tensors (Sec. IV C). Also, the use of the frozen core approximation may lie on the origin of a looser agreement. For the ^{33}S interaction, it may be expected that core polarization may add an important contribution. For the ligand interactions, it is striking that the isotropic superhyperfine constant is very well calculated when the s orbitals of the neighboring ion exhibit a non-zero overlap with the unpaired electron orbital [Rb(1) ions for S_2^- in the $^2B_{2g}$ ground state, Br($Z3$) and I($Z3$) ions for S_2^- in the $^2B_{3g}$ ground state], while for ions in the nodal planes of the unpaired electron orbital, the agreement with experiment is much worse. For the latter ions, the isotropic superhyperfine value is expected to be dominated by core polarization effects. Furthermore, the underestimation of the anisotropic part of the Rb(1) superhyperfine tensor in RbCl may indicate that the delocalization of the unpaired electron distribution is underestimated by the calculations. This is most probably a result of the limited accuracy in the quantum mechanical representation of the ions in the cluster. The fact that important contributions to the anisotropic superhyperfine tensors of the Na(1) and Na(2) ions in sodium halides appear to be neglected [as a result of which, e.g., the calculated tilting angle of the Na(1) superhyperfine tensor does not agree at all with experiment] may also point in this direction. Finally, the underestimation of overlap and covalency effects in our calculations also appear to be reflected in a systematic overestimation of the g_z values (see Table V). In Eq. (6) it is shown that overlap and covalency effects ($l<1$) tend to decrease the g_z value, while they have no first order influence on g_x and g_y. The other parameters (E,Δ,λ) influence all three *g* factors. For the S_2^- ions with the $^2B_{2g}$ ground state, calculated g_x and g_y values are always too small compared with experiment, while the calculated g_z values are larger than the experimental values. The numerical discrepancies are therefore most probably mainly due to an overestimation of λ/E and λ/Δ. For the S_2^- ions in the $^2B_{3g}$ ground state, on the other hand, no systematic discrepancies can be found in g_x and g_y, but the calculated g_z value is always too large in comparison with experiment. The ligand field expressions for the principal g components in Eq. (6) suggest that the calcu-

TABLE XI. Experimental and theoretical isotropic and anisotropic *A* tensor values (MHz) of Rb(1) and Rb(2) (^{85}Rb) for RbCl. A_{iso} stands for isotropic part, while $A_{\text{i,aniso}}$ ($i=x,y,z$) stands for the anisotropic part of the *A* tensor. The angle α_A is in degrees.

	Experimental		Theoretical	
	Rb(1) [a]	Rb(2) [a]	Rb(1)	Rb(2)
$A_{x,\text{aniso}}$	8.87	0	3.32	0.01
$A_{y,\text{aniso}}$	−3.91	0.28	−1.21	0.1
$A_{z,\text{aniso}}$	−4.96	−0.28	−2.11	−0.11
A_{iso}	25.73	−1.38	25.42	0.06
α_{A}	32.9	0	29.4	0

[a]Reference 14.

TABLE XII. Experimental and calculated Q tensor values (MHz) of Rb(1) Rb(2) (^{85}Rb) for RbCl. The angle α_{Q} is in degrees.

	Experimental		Theoretical	
	Rb(1) [a]	Rb(2) [a]	Rb(1)	Rb(2)
Q_x	−0.53	−0.27	−0.63	0.07
Q_y	0.02	0.16	0.27	−0.02
Q_z	0.51	0.11	0.36	−0.05
α_Q	36.7	0	35.2	0

[a]Reference 14.

lations overestimate the l parameter, or, in other words, underestimate the effect of covalency and overlap.

In spite of the limitations discussed above, our approach for simulating S_2^- defects in MZ lattices has proven to be very successful. Using the same defect model and the same quantum mechanical description of the defect in the lattice, the correct ground state was found for the eight MZ lattices, in which only one S_2^- defect is known. The numerical agreement between calculated and experimental g values is in each case very satisfactory and in the case of S_2^- defects in the $^2B_{3g}$ ground state, nearly perfect. Calculated ^{33}S hyperfine tensors are always in very good qualitative agreement with experiment. The correspondence between calculations and experiment should not be regarded as being fortuitous. Indeed, the statistical chance of obtaining the right ground state for the S_2^- defect in all eight MZ lattices is only $(\frac{1}{2})$.[8] The DFT results thus strongly indicate that the monovacancy model for the defect in these lattices is correct and that the applied cluster in vacuo model for the defect is very adequate, although further improvement in the calculation of the spin Hamiltonian parameters of the neighboring ions is still desirable. Furthermore, our calculations have shown that one of the S_2^- defects in KCl can certainly not be assigned to a monovacancy model without considering other neighboring lattice defects (S_2^- with the $^2B_{3g}$ ground state), while the paramagnetic properties of the second (S_2^- with the $^2B_{2g}$ ground state) correspond very well to those calculated for S_2^- in a Cl^- monovacancy. The cluster in vacuo approach followed in this study thus appears very attractive for the validation of microscopic models for chalcogen defects in alkali halides. Its merits and limitations will be further explored in DFT-EPR calculations for other paramagnetic defects (e.g., X^- or X_3^-) in these lattices.

VII. CONCLUSION

In the performed DFT-EPR study, the calculated magnetic resonance parameters of the S_2^- molecular ion were compared with results of EPR and ENDOR single crystal measurements for nine alkali halide lattices. A first major success of the present DFT work is the correct prediction of all ground states, using the same procedure and level of theory for all lattices. All calculations were performed assuming a monovacancy model and hence give conclusive support for the latter model. In the KCl lattice, this allows us to assign one of the experimentally observed S_2^- defects to a monovacancy model, while for the other this model is inadequate. The 88-atom cluster provides an excellent compromise between computational feasibility, on the one hand, and the quality of the environmental description on the other hand. The quantitative agreement between calculated and experimental magnetic resonance parameters can, in general, be called very satisfactory. The best quantitative results were obtained for the g tensor, the ^{33}S hyperfine tensor and the nearest halogen interactions in NaBr and NaI. For the latter this also includes the orientations of the principal A and Q tensor axes.

The interactions with the nearest cation neighbors still pose considerable problems. The calculation of the superhyperfine tensor axes and isotropic hyperfine couplings is a great challenge for future DFT calculations, which are in progress for O_2^-, Se_2^-, and SSe^-. As a general conclusion, the calculations can be used to analyze experimental EPR and ENDOR data and demonstrate the power of DFT methods in the study of defects in ionic crystals.

ACKNOWLEDGMENTS

This work was supported by the Fund for Scientific Research (FWO-Flanders, Belgium).

*Author to whom all correspondence should be addressed: Professor Dr. F. Callens, Ghent University, Department of Solid State Sciences, Krijgslaan 281 - S1, B-9000 Ghent, Belgium. Fax: +32 9 264 49 96. Email address: freddy.callens@rug.ac.be

[1] W. Känzig and M.H. Cohen, Phys. Rev. Lett. **3**, 509 (1959).
[2] R. Zeller and W. Känzig, Helv. Phys. Acta **40**, 845 (1967).
[3] R.T. Shuey and H.R. Zeller, Helv. Phys. Acta **40**, 873 (1967).
[4] J.R. Morton, J. Chem. Phys. **43**, 3418 (1965).
[5] J.R. Morton, J. Phys. Chem. **71**, 89 (1967).
[6] L.E. Vannotti and J.R. Morton, Phys. Rev. **161**, 282 (1967).
[7] L.E. Vannotti and J.R. Morton, Phys. Lett. **24A**, 250 (1967).
[8] F. Callens, P. Matthys, and E. Boesman, Phys. Status Solidi B **118**, K35 (1983).
[9] P. Matthys, F. Callens, and E. Boesman, Solid State Commun. **45**, 1 (1983).
[10] F. Callens, F. Maes, P. Matthys, and E. Boesman, J. Phys.: Condens. Matter **1**, 6912 (1989).
[11] F. Maes, F. Callens, P. Matthys, and E. Boesman, J. Phys. Chem. Solids **51**, 1289 (1990).
[12] F. Maes, F. Callens, P. Matthys, and E. Boesman, Phys. Status Solidi B **161**, K1 (1990).
[13] F. Maes, P. Matthys, F. Callens, P. Moens, and E. Boesman, J. Phys.: Condens. Matter **4**, 149 (1992).
[14] S. Van Doorslaer, F. Maes, F. Callens, P. Moens, and E. Boesman, J. Chem. Soc., Faraday Trans. **90**, 2541 (1994).
[15] S. Van Doorslaer, F. Callens, F. Maes, and P. Matthys, J. Phys.: Condens. Matter **7**, 9279 (1995).
[16] S. Van Doorslaer, F. Callens, F. Maes, and E. Boesman, Phys. Rev. B **54**, 1145 (1996).
[17] S. Van Doorslaer, F. Maes F. Callens, P. Matthys, and E. Boesman, J. Chem. Soc., Faraday Trans. **92**, 1579 (1996).
[18] S. Patchkovskii and T. Ziegler, J. Chem. Phys. **111**, 5730 (1999).
[19] M. Munzarová and M. Kaupp, J. Phys. Chem. A **103**, 9966 (1999).
[20] E. van Lenthe and A. van der Avoird, J. Phys. Chem. A **104**, 2070 (2000).
[21] M.L. Munzarová, P. Kubacek, and M. Kaupp, J. Am. Chem. Soc. **122**, 11 900 (2000).
[22] S. Patchkovskii and T. Ziegler, J. Am. Chem. Soc. **122**, 3506 (2000).
[23] P.J. Bruna and F. Grein, Int. J. Quantum Chem. **77**, 324 (2000).
[24] M. Stein, E. van Lenthe, E.J. Baerends, and W. Lubitz, J. Phys. Chem. A **105**, 416 (2001).

[25] F. Neese, J. Phys. Chem. A **105**, 4290 (2001).
[26] C. Quintanar, M. Garcia, M. Martinez, M. Castro, J.L. Boldu, E. Munoz, and P.R. Taylor, Int. J. Quantum Chem. **79**, 34 (2000).
[27] A.A. Leitao, J.A. Coelho Neto, N.M. Pinhal, C.E. Bielschowsky, and N.V. Vugman, J. Phys. Chem. A **105**, 614 (2001).
[28] C. Kölmel and C. Ewig, J. Phys. Chem. B **105**, 8538 (2001).
[29] G. Mallia, R. Orlando, C. Roetti, P. Ugliengo, and R. Dovesi, Phys. Rev. B **63**, 235102 (2001).
[30] L.A. Eriksson, O.L. Malkina, V.G. Malkin, and D.R. Salahub, J. Chem. Phys. **100**, 5066 (1994).
[31] M.A. Austen, L.A. Eriksson, and R.J. Boyd, Can. J. Chem. **72**, 695 (1994).
[32] G. Schreckenbach and T. Ziegler, J. Phys. Chem. A **101**, 3388 (1997).
[33] P.J. Bruna and F. Grein, J. Phys. Chem. A **102**, 3141 (1998).
[34] F. Ban, S.D. Wetmore and R.J. Boyd, J. Phys. Chem. A **103**, 4303 (1999).
[35] P. Lahorte, F. De Proft, G. Vanhaelewyn, B. Masschaele, P. Cauwels, F. Callens, P. Geerlings, and W. Mondelaers, J. Phys. Chem. A **103**, 6650 (1999).
[36] P. Lahorte, F. De Proft, F. Callens, P. Geerlings, and W. Mondelaers, J. Phys. Chem. A **103**, 11 130 (1999).
[37] A.R. Jaszewski, J. Jezierska, and A. Jezierski, Chem. Phys. Lett. **319**, 611 (2000).
[38] M. Engström, A. Gräslund, B. Minaev, O. Vahtras, and H. Agren, J. Phys. Chem. A **104**, 5149 (2000).
[39] P.J. Bruna, G.H. Lushington, and F. Grein, J. Mol. Struct. **527**, 139 (2000).
[40] E. Pauwels, V. Van Speybroeck, P. Lahorte, and M. Waroquier, J. Phys. Chem. A **105**, 8794 (2001).
[41] H. C. Box, *Radiation Effects: ESR and ENDOR Analysis* (Academic Press, New York, 1977), pp. 54–59.
[42] N. M. Atherton, *Principals of Electron Spin Resonance* (Prentice Hall, New York, 1993).
[43] J. A. Weil, J. R. Bolton, and J. E. Wertz, *Electron Paramagnetic Resonance, Elementary Theory and Practical Applications*, (Wiley, New York, 1994).
[44] J. E. Harriman, *Theoretical Foundations of Electron Spin Resonance* (Academic Press, New York, 1978).
[45] R. G. Parr and W. Yang, *Density Functional Theory of Atoms and Molecules* (Oxford University Press, Oxford, 1989).
[46] T. Ziegler, Chem. Rev. **91**, 651 (1991).
[47] D. R. Salahub, M. Castro, and E. Y. Proynov, in *Relativistic and Electron Correlation Effects in Molecules and Solids*, edited by G. L. Malli (Plenum New York, 1994).
[48] ADF, http://tc.chem.vu.nl/SCM., Department of Theoretical Chemistry, Vrije Universiteit Amsterdam.
[49] E.J. Baerends, D.E. Ellis, and P. Ros, Chem. Phys. **2**, 41 (1973).
[50] F. Guerra, O. Visser, J. G. Snijders, G. te Velde, and E. J. Baerends, Methods and Techniques in Computational Chemistry METECC-95, E. Clementi, G. Corongiu, Cagliari 1995, pp. 305–395.
[51] E. van Lenthe, P. Wormer, and A. van der Avoird, J. Chem. Phys. **107**, 2488 (1997).
[52] E. van Lenthe, A. van der Avoird, and P. Wormer, J. Chem. Phys. **108**, 4783 (1997).
[53] E. van Lenthe and E.J. Baerends, J. Chem. Phys. **112**, 8279 (2000).
[54] All standard ADF basis sets are available on the net at http://www.scm.com/Doc/atomidata.
[55] S.H. Vosko, L. Wilk, and M. Nusair, Can. J. Phys. **58**, 1200 (1980).
[56] R. van Leeuwen and E.J. Baerends, Phys. Rev. A **49**, 2421 (1994).
[57] J.P. Perdew, J.A. Chevary, S.H. Vosko, K.A. Jackson, M.R. Pederson, D.J. Singh, and C. Fiolhais, Phys. Rev. B **46**, 6671 (1992).
[58] C. Lee, W. Yang and R.G. Parr, Phys. Rev. B **37**, 785 (1988).
[59] B.G. Johnson, P.M.W. Gill, and J.A. Pople, J. Chem. Phys. **98**, 5612 (1993).
[60] C. Chang, M. Pelissier, and P. Durand, Phys. Scr. **34**, 394 (1988).
[61] J-L. Heully, I. Lindgren, E. Lindroth, S. Lundqvist, and A.M. Martensson-Pendrill, J. Phys. B **101**, 1272 (1994).
[62] E. van Lenthe, E.J. Baerends, and J.G. Snijders, J. Chem. Phys. **99**, 4597 (1993).
[63] E. van Lenthe, E.J. Baerends, and J.G. Snijders, J. Chem. Phys. **101**, 9783 (1994).
[64] E. van Lenthe, J.G. Snijders, and E.J. Baerends, J. Chem. Phys. **105**, 6505 (1996).
[65] E. van Lenthe, R.v. Leeuwen, E.J. Baerends, and J.G. Snijders, Int. J. Quantum Chem. **57**, 281 (1996).
[66] E. van Lenthe, A.E. Ehlers, and E.J. Baerends, J. Chem. Phys. **110**, 8943 (1999).
[67] E. van Lenthe, A. van der Avoird, and P. Wormer, J. Chem. Phys. **108**, 4783 (1998).
[68] F. Herman and F. Skilman, *Atomic Structure calculations* (Prentice-Hall, Englewood Cliffs, NJ, 1963).
[69] R.E. Crandall, Exp. Math. **8**, 367 (1999).
[70] C.G.V. de Walle and P.E. Blöchl, Phys. Rev. B **47**, 4244 (1993).